

Anomalous convective flows carve pinnacles and scallops in melting ice

Scott Weady¹, Joshua Tong^{1,2}, Alexandra Zidovska² & Leif Ristroph^{1*}

¹*Applied Math Lab, Courant Institute, New York University, New York NY 10012 USA*

²*Department of Physics, New York University, New York NY 10003 USA*

(Dated: May 31, 2022)

We report on the shape dynamics of ice suspended in cold fresh water and subject to the natural convective flows generated during melting. Experiments reveal shape motifs for increasing far-field temperature: Sharp pinnacles directed downward at low temperatures, scalloped waves for intermediate temperatures between 5 and 7°C, and upward pointing pinnacles at higher temperatures. Phase-field simulations reproduce these morphologies, which are closely linked to the anomalous density-temperature profile of liquid water. Boundary layer flows yield pinnacles that sharpen with accelerating growth of tip curvature while scallops emerge from a Kelvin-Helmholtz-like instability caused by counterflowing currents that roll up to form vortex arrays. These results show how the molecular-scale effects underlying water’s density anomaly are imprinted at macro-scales on melting ice through intricate flows.

The shape of a landform or landscape holds clues to its history and the environmental conditions under which it developed. However, interpreting geological morphologies is challenging due to the complex multi-scale and interactive processes that form them, such as erosion and deposition, dissolution and solidification, and melting and freezing [1–6]. The latter yield examples across scales, including rippled icicles, pinnacle shaped icebergs, textured ice caves, and larger icescapes [7–12]. Understanding how to interpret such forms and the physical mechanisms behind them is all the more important due to the increasing melt rate of the Earth’s ice reserves.

Melting is an example of a Stefan problem, which classically seeks to determine interface motion induced by a phase transition [13]. Here the solid-liquid interface recedes due to heat conduction along temperature gradients, and the energy released during phase change in turn modifies the temperature field in the fluid. In many situations, these temperature changes cause density variations that drive gravitational convective flows, which also feed back on the interface motion [14, 15]. This convective Stefan problem has recently been studied in the related context of solids dissolving into liquids, where the effects of flows due to solutal convection can be seen in fine-scale surface features and overall forms [16–18].

Convective flows are well studied in heat transfer problems involving fixed boundaries [19, 20], but the effects of shape-flow coupling are less understood. The problem is uniquely complex for melting ice due to the unusual effect of temperature on liquid water’s density, which displays a maximum at about 4°C. This so-called density anomaly, while ultimately a molecular-scale effect that leads to relative density differences on the order of 0.01%, nonetheless strongly affects convective flows, heat transfer characteristics, and hydrodynamic instabilities across a wide range of scales [21–27].

Here we show that the density anomaly and consequent flows are imprinted onto the shape of melting ice. We consider the highly simplified context of ice sub-

merged within fresh water while subject to the convective flows generated during melting. Reporting first on experiments, we manufacture clear ice with a directional freezing method and immerse it in water of fixed far-field temperature $T_\infty \in [2, 10]^\circ\text{C}$. We focus on cylindrical initial forms that are sized, supported, and oriented to allow for observation of the long-time shape dynamics. Using a large tank in a cold room facility, the far-field water temperature is tightly controlled and systematically varied to assess its impact on shape development, as captured by time-lapse photography. Complete experimental details are available as Supplemental Material.

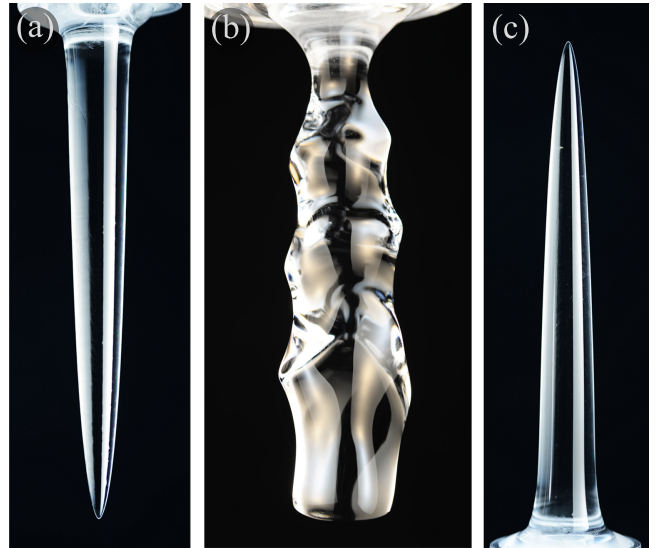


FIG. 1. Representative morphologies formed by melting ice in laboratory experiments. (a) For sufficiently cold ambient temperatures $T_\infty \lesssim 5^\circ\text{C}$ (here 4.0°C), the ice tapers from below to form an inverted pinnacle. (b) For intermediate temperatures $5^\circ\text{C} \lesssim T_\infty \lesssim 7^\circ\text{C}$ (5.6°C), scalloped patterns of typical wavelength 2–4 cm form on the surface. (c) Upright pinnacles form for warmer temperatures $T_\infty \gtrsim 7^\circ\text{C}$ (8.0°C). Photographs capture the late-stage ice removed from water and under diffuse lighting. Scale: the pieces measure about 1 cm where attached to their supports.

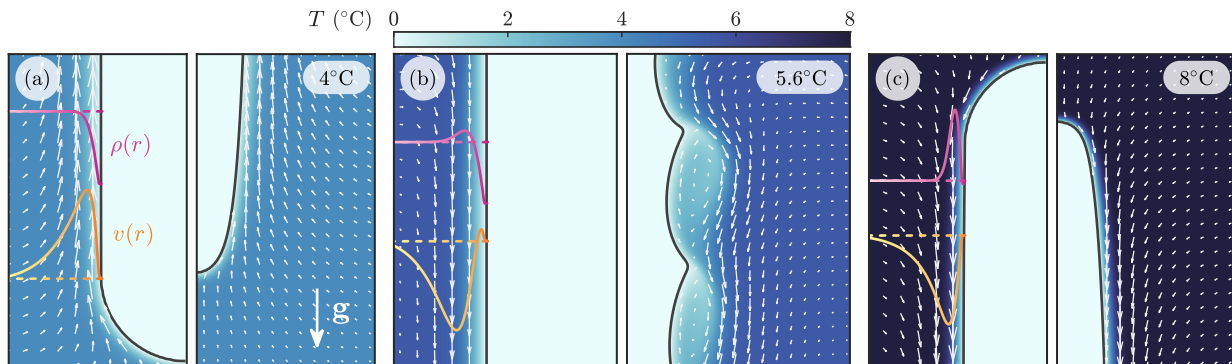


FIG. 2. Flow velocity (arrows) and temperature (color) fields from phase-field simulations for (a) $T_\infty = 4^\circ\text{C}$, (b) 5.6°C , and (c) 8°C at early (left) and late (right) times. Curves show the flow speed (yellow) and density (pink) profiles at early times. Melting in cold water is associated with upward flow and downwards tapering of the ice as in (a), whereas warmer temperatures involve downwards flow and tapering at the top as in (c). Intermediate temperatures yield shear flows involving rising fluid near the surface and sinking outer flows, driving an instability that later patterns the surface.

We first present some motivating observations from experiments, which reveal three distinct morphologies that arise for specific intervals of the far-field temperature. Representative photographs are shown in Fig. 1. For sufficiently low temperatures $T_\infty \lesssim 5^\circ\text{C}$, the ice becomes tapered, thinning at its lower end to form an inverted pinnacle with apex oriented downward, as shown in panel (a). (If supported at its bottom, tapering causes the piece to pinch off near the support, preventing observation of the long-time dynamics.) At higher temperatures $T_\infty \gtrsim 7^\circ\text{C}$, a similarly shaped pinnacle forms but with upright orientation, as seen in (c). For intermediate temperatures $5^\circ\text{C} \lesssim T_\infty \lesssim 7^\circ\text{C}$, wavy or scalloped features pattern the ice surface, as shown in (b).

The sensitive dependence of shape on temperature evokes water's anomalous density-temperature profile, whose peak at $T_* \approx 4^\circ\text{C}$ suggests distinct scenarios categorized by the far-field temperature T_∞ . For sufficiently warm temperatures $T_\infty \gtrsim 2T_*$, the cold liquid near the surface is uniformly denser than that in the far-field and is expected to sink. For cold temperatures $T_\infty < T_*$, however, the density anomaly upends intuition: Cold liquid near the surface is less dense and will rise. Intermediate temperatures $T_\infty \in [T_*, 2T_*]$ are more subtle, since the coldest fluid near the surface is less dense than that in the far field, while fluid slightly further away from the surface must be at or near T_* and is thus more dense. Hence the emergent flows are not easily inferred.

To more clearly interpret the observed morphologies, we formulate and implement simulations of the shape dynamics coupled to the flow and temperature fields. Here we use the phase-field model [28, 29], which has proven successful for moving boundary problems with natural convection [30–32]. Material is implicitly represented by a continuous phase parameter $\phi(\mathbf{x}, t)$, which takes values $\phi = 0$ in the solid phase and $\phi = 1$ in the liquid, with the interface defined as the level set $\phi = 1/2$. This phase parameter is then used to describe energy contributions from phase change and to approximate the no-slip

boundary condition on the ice, while admitting numerical discretization on a Cartesian grid. Introducing the quadratic equation of state $\rho(T) = \rho_*[1 - \beta(T - T_*)^2]$ as a basic model for the density anomaly [21, 23], the fluid motion is described by the Navier-Stokes equation in the Boussinesq approximation

$$\frac{D\mathbf{u}}{Dt} = \text{Pr} \left(-\nabla p + \Delta \mathbf{u} + \text{Ra} \theta^2 \hat{\mathbf{z}} \right) - \eta(1 - \phi)^2 \mathbf{u}, \quad (1)$$

$$\nabla \cdot \mathbf{u} = 0, \quad (2)$$

where $\mathbf{u}(\mathbf{x}, t)$ is the velocity, $p(\mathbf{x}, t)$ is the pressure, and $\theta(\mathbf{x}, t) = (T(\mathbf{x}, t) - T_*) / (T_\infty - T_0)$ is the dimensionless temperature with $T_0 = 0^\circ\text{C}$ the melting temperature. Parameters include the Rayleigh number $\text{Ra} = g\beta(T_\infty - T_0)^2 H^3 / \nu \kappa_T$, which compares buoyant and viscous forces, and the Prandtl number $\text{Pr} = \nu / \kappa_T$, which assesses viscous and thermal diffusivities. Here g is acceleration due to gravity, H is the initial height of the ice, ν is the fluid viscosity, and κ_T is the thermal diffusivity. The last term in (1) is a Brinkman penalization force that models the ice as a porous medium, in which the velocity vanishes for large resistivity $\eta \gg 1$ [33].

Following the thermodynamic derivation in [30], the temperature field and phase parameter follow the evolution equations

$$\frac{D\theta}{Dt} = \Delta \theta - \frac{1}{\text{St}} \frac{df}{d\phi} \frac{\partial \phi}{\partial t}, \quad (3)$$

$$\frac{\partial \phi}{\partial t} = m \Delta \phi + \frac{m(\theta - \theta_0)}{\delta^2} \frac{df}{d\phi} - \frac{m}{4\delta^2} \frac{dg}{d\phi}. \quad (4)$$

The last term in Eq. (3) captures energy contributions from phase change, the magnitude of which is controlled by the Stefan number $\text{St} = c_p(T_\infty - T_0) / \mathcal{L}$, with c_p the heat capacity and \mathcal{L} the latent heat of fusion. In Eq. (4), m is a regularization parameter, δ is an effective interface thickness, $\theta_0 = (T_0 - T_*) / (T_\infty - T_0)$ is the dimensionless melting temperature, and the functions $f(\phi) = \phi^3(10 - 15\phi + 5\phi^2)$ and $g(\phi) = \phi^2(1 - \phi)^2$ are

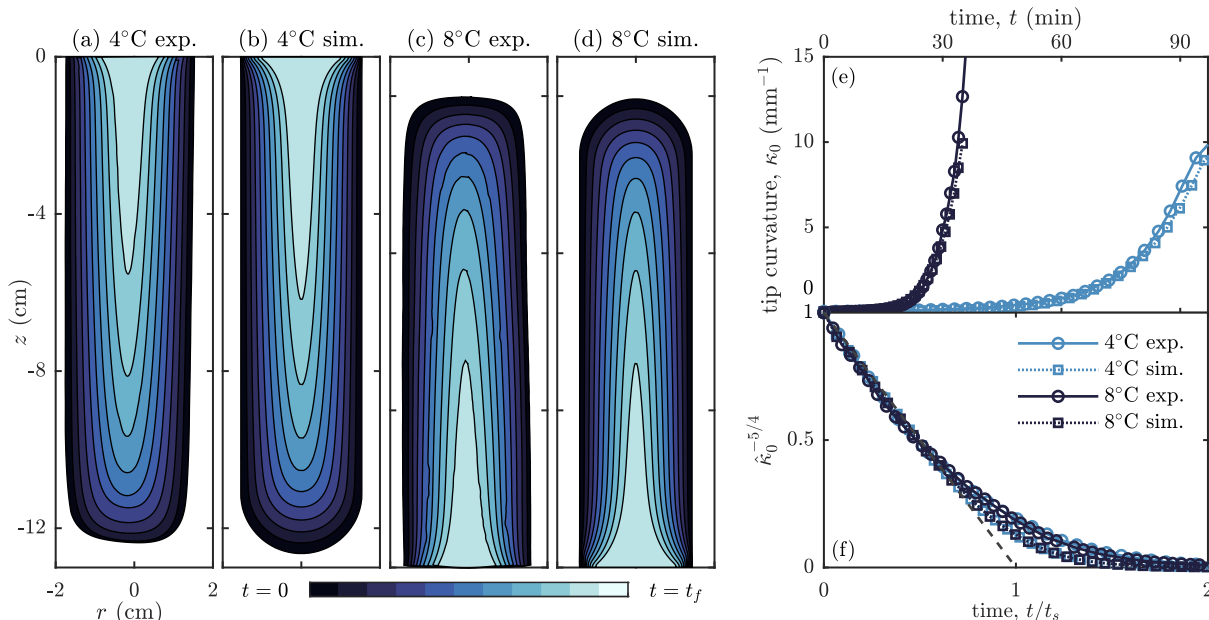


FIG. 3. Dynamics of pinnacle formation. Panels (a)-(d) show interfaces for $T_\infty = 4^\circ\text{C}$ and $T_\infty = 8^\circ\text{C}$ extracted over time (dark to light blue) in experiments and simulations. The corresponding tip curvatures are plotted in (e), which exhibit rapid sharpening to micro-scales. At early times, all data follow the scaling law $\kappa_0(t) = \kappa_0(0)(1 - t/t_s)^{-4/5}$, as shown in (f) by the linear behavior $1 - t/t_s$ of the transformed quantity $[\hat{\kappa}_0(t/t_s)]^{-5/4} = [\kappa_0(t/t_s)/\kappa_0(0)]^{-5/4}$.

potentials that ensure no phase-change occurs away from the interface. In the limit $\delta \rightarrow 0$ and $\eta \rightarrow \infty$, the system (1)-(4) recovers the Navier-Stokes equations with no-slip boundary conditions on the ice and the Stefan condition for the interface velocity $V_n = \text{St} \partial\theta/\partial n$ [30].

For comparison with the cylindrical geometries in experiments, we solve the system of equations (1)-(4) on an axisymmetric domain sufficiently wide such that the far-field temperature remains constant to within 0.1°C . Estimated from the experimental parameters, the Prandtl number is $\text{Pr} = 12$ and the Rayleigh number $\text{Ra}/T_\infty^2 = 2.5 \times 10^6$. The selected Stefan number $\text{St}/T_\infty = 0.05$ is larger than that estimated for experiments, which reduces simulation run time while having negligible effect on the overall shape dynamics. Implementation details can be found in the Supplemental Material.

Fig. 2 shows the interfaces at early and late times for three representative values of T_∞ . Also shown are the flow velocity and temperature fields as well as curves representing the density and velocity profiles along a horizontal transect at early times, the latter substantiating our inferences based on the density anomaly. For $T_\infty = 4^\circ\text{C}$, shown in panel (a), an upward boundary layer flow persists for all times. This flow is fed by warmer outer fluid that is continuously entrained from the sides and bottom, offering a mechanism for the enhanced melt rate that tapers the ice from below. For $T_\infty = 8^\circ\text{C}$, shown in (c), the situation is similar but inverted: A downward boundary layer flow tapers the top of the ice to form an upright pinnacle. For the intermediate case

$T_\infty = 5.6^\circ\text{C}$, shown in (b), early times are marked by a thin region of upward flow near the surface surrounded by a broader region of downward flow. This shear flow eventually destabilizes and forms recirculating vortices that entrain the warmer outer fluid and carve scallop-shaped indentations. Across all cases, stagnation points of the flow are associated with sharp features of the surface, including the apexes of the pinnacles and cusped crests of the scalloped waves.

Further analysis of the experiments and simulations provides insight into the mathematical structure of the shape dynamics. Considering first the pinnacles observed for sufficiently low or high T_∞ , we show in Fig. 3(a)-(d) comparisons of the shape progression as measured in experiments and computed in simulations for $T_\infty = 4^\circ\text{C}$ and 8°C . The strong agreement across all times (dark to light blue) serves as a cross-validation of the simulations and experiments and demonstrates the robustness of the pinnacle form. These pinnacles are reminiscent of those recently observed for bodies dissolving in natural convective flows [15–17], for which a boundary layer theory analysis predicts that the pinnacle apex sharpens via a power law growth of curvature: $\kappa_0(t) = \kappa_0(0)(1 - t/t_s)^{-4/5}$ [17, 20]. Here $\kappa_0(0)$ is the initial tip curvature and t_s is the blow-up time for the predicted singular dynamics, which were shown to accurately describe the initial stages of sharpening during dissolution.

To test this law, we extract the interfaces over time from experiments and simulations and evaluate the apex curvature by fitting and differentiating a fourth-order

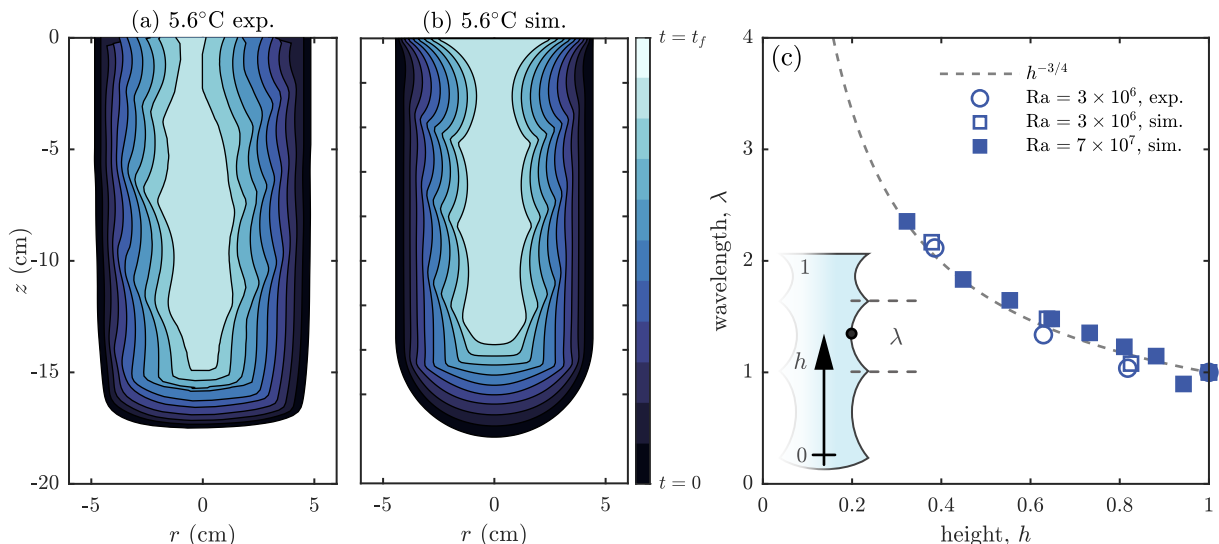


FIG. 4. Dynamics of scallop formation. Panels (a) and (b) show extracted interfaces over time for $T_\infty = 5.6^\circ\text{C}$ in experiment and simulation, respectively. Panel (c) plots the cusp-to-cusp wavelength of the scallops versus their vertical location or height, confirming the scaling $\lambda \propto h^{-3/4}$ predicted by an analysis of the viscous Kelvin-Helmholtz instability. Additional simulations (filled squares) for a taller body and thus higher Ra confirm the trend over wider ranges of the variables.

polynomial for the tip height as a function of radius. Strikingly, the tip curvature $\kappa_0(t)$, shown in Fig. 3(e), exhibits steep and seemingly unbounded growth. The radius of curvature reaches values smaller than 100 microns, as fine as a human hair and approaching the resolutions of the experiments and simulations. In panel (f) we plot the rescaled quantity $[\hat{\kappa}_0(t/t_s)]^{-5/4} = [\kappa_0(t/t_s)/\kappa_0(0)]^{-5/4}$. Remarkably, all data collapse to the predicted linear form $1 - t/t_s$ (dashed line) for early times, indicating a mechanism shared with dissolution for the formation of ultra-sharp structures [17]. The curvature continues to grow at later times but falls off the singular pace.

Experiments and simulations are also in close agreement for intermediate temperatures, yielding scallops of comparable scales as seen in Figs. 4(a) and (b) for $T_\infty = 5.6^\circ\text{C}$. Some disparities are expected as the simulations are axisymmetric while the patterns are three-dimensional in experiments. Nonetheless, the wave-like structures common to both are indicative of a hydrodynamic instability. Shear flows of the form observed in Fig. 2(b) are known to undergo the Kelvin-Helmholtz instability, the classic analysis of which involves counter-flowing layers of inviscid fluid [34, 35]. Such flows are unstable, with the smallest wavelengths growing at the fastest rates. Viscosity, however, suppresses high frequency modes, yielding a most unstable wavelength $\lambda \sim \text{Re}^{-1/2}$, where Re is the Reynolds number [36, 37]. While Re is somewhat poorly defined since the flows accelerate along the surface, scaling arguments predict $\text{Re} \sim \text{Ra}^{1/2}$ for $\text{Ra} \gg 1$ [38], with experimental evidence suggesting an exponent slightly below 1/2 [39, 40]. Observing that $\text{Ra} \sim h^3$, where h is the vertical distance from the bot-

tom of the ice, we predict the wavelength decreases up the surface of the ice as $\lambda \sim h^{-3/4}$.

This scaling law can be used to test the hypothesis that the maximally unstable wavelength of the shear flow is imprinted on the ice in the form of scalloped waves. We determine the locations of the wave crests at early times and identify the wavelength λ with differences between successive crests and the height h with their midpoint. Figure 4(c) shows results from experiments (open circles) and simulations (open squares) at $T_\infty = 5.6^\circ\text{C}$. Here, h is normalized by the total height and λ by its value at $h = 1$, and the location of $h = 0$ is treated as a fitting parameter due to the ambiguous location of the lowest scallop. Over the few wavelengths present, the data indeed follow the $-3/4$ scaling law. Additional simulations of taller ice (filled squares), details of which are given in the Supplemental Material, yield more wavelengths and correspondingly more convincing agreement.

This work identifies three shape motifs of melting ice and their physical origins in natural convective flows, shape-flow coupling, and the density anomaly. Sharply-pointed pinnacles directed downwards for $T_\infty \lesssim 5^\circ\text{C}$ and upwards for $T_\infty \gtrsim 7^\circ\text{C}$ are formed by persistent, directional boundary layer flows, which are analogous to the flows that form pinnacles in dissolution under solutal convection [15–18]. These observations may also relate to the pinnacle morphology of icebergs, which has been attributed to natural convective flows but has not previously been validated through models or simulations, nor realized in lab experiments [11, 41]. In contrast, the scalloped waves observed here for $5^\circ\text{C} \lesssim T_\infty \lesssim 7^\circ\text{C}$ have their origin in the buoyant rise of cold water near the sur-

face, the sinking of warmer water further outward in the boundary layer, and the resulting shear flows that destabilize and roll up into vortices. Similar patterning on icebergs, ice shelves, and bore holes has been attributed to instabilities induced by externally-driven flows or double-diffusive convection [7, 42–44]. Our results reveal a previously unknown mechanism involving the intrinsic flows generated by water’s anomalous density characteristics. Future studies might assess the interplay and relative contributions of all these mechanisms for different environmental conditions and parameter regimes.

Even in the idealized context studied here, the shapes and flows exhibit an impressive range of scales. Stable boundary layer flows approximately 1 cm thick sculpt tall pinnacles with micro-scale apex curvatures, and shear instabilities in the boundary layer carve scallops of variable wavelength, broad troughs, and sharply cusped peaks. Ultimately, these emergent features are rooted in the molecular-scale interactions that give liquid water its anomalous thermophysical properties.

* ristroph@cims.nyu.edu

- [1] J. M. Huang, M. N. J. Moore, and L. Ristroph, *Journal of Fluid Mechanics* **765**, R3 (2015).
- [2] W. W. Mullins and R. F. Sekerka, *Journal of Applied Physics* **34**, 323 (1963).
- [3] J. S. Wettlaufer, M. G. Worster, and H. E. Huppert, *Journal of Fluid Mechanics* **344**, 291–316 (1997).
- [4] L. Ristroph, M. N. J. Moore, S. Childress, M. J. Shelley, and J. Zhang, *Proceedings of the National Academy of Sciences* **109**, 19606 (2012).
- [5] J. N. Hewett and M. Sellier, *Journal of Fluids and Structures* **70**, 295 (2017).
- [6] E. Nakouzi, R. E. Goldstein, and O. Steinbock, *Langmuir: the ACS journal of surfaces and colloids* **31** (2015), 10.1021/la503562z.
- [7] R. Curl, *Trans. Cave Res. Group* **7**, 121 (1966).
- [8] S. Kobayashi, *Contributions from the Institute of Low Temperature Science* **A29**, 1 (1980).
- [9] J. A. Neufeld, R. E. Goldstein, and M. G. Worster, *Journal of Fluid Mechanics* **647**, 287–308 (2010).
- [10] C. Camporeale and L. Ridolfi, *Journal of Fluid Mechanics* **694**, 225–251 (2012).
- [11] Y. A. Romanov, N. A. Romanova, and P. Romanov, *Antarctic Science* **24**, 77–87 (2012).
- [12] S. Filhol and M. Sturm, *Journal of Geophysical Research: Earth Surface* **120**, 1645 (2015).
- [13] L. I. Rubenstein, *The Stefan Problem* (American Mathematical Society, 1971).
- [14] L. Ristroph, *Journal of Fluid Mechanics* **838**, 1–4 (2018).
- [15] S. S. Pegler and M. S. Davies Wykes, *Journal of Fluid Mechanics* **915**, A86 (2021).
- [16] M. S. Davies Wykes, J. M. Huang, G. A. Hajjar, and L. Ristroph, *Phys. Rev. Fluids* **3**, 043801 (2018).
- [17] J. M. Huang, J. Tong, M. Shelley, and L. Ristroph, *Proceedings of the National Academy of Sciences* **117**, 23339 (2020).
- [18] S. S. Pegler and M. S. Davies Wykes, *Journal of Fluid Mechanics* **900**, A35 (2020).
- [19] D. J. Tritton, *Physical Fluid Dynamics* (Springer Netherlands, 1977).
- [20] H. Schlichting and G. K., *Boundary layer theory* (Springer, Berlin, Heidelberg, 2017).
- [21] G. Veronis, *Astrophysical Journal* **137**, 641 (1962).
- [22] J. M. Higgins and B. Gebhart, *Journal of Heat Transfer* **105**, 767 (1983).
- [23] S. Toppaladoddi and J. S. Wettlaufer, *Phys. Rev. Fluids* **3**, 043501 (2018).
- [24] M. S. Bendell and B. Gebhart, *International Journal of Heat and Mass Transfer* **19**, 1081 (1976).
- [25] T. Saitoh, *Applied Scientific Research* **32** (1976), 10.1007/BF00385849.
- [26] B. Gebhart and T. Wang, *Chemical Engineering Communications* **13**, 197 (1982).
- [27] D. White, R. Viskanta, and W. Leidenfrost, *Experiments in Fluids* **4**, 171 (1986).
- [28] S.-L. Wang, R. Sekerka, A. Wheeler, B. Murray, S. Coriell, R. Braun, and G. McFadden, *Physica D: Non-linear Phenomena* **69**, 189 (1993).
- [29] C. Beckermann, H.-J. Diepers, I. Steinbach, A. Karma, and X. Tong, *Journal of Computational Physics* **154**, 468 (1999).
- [30] B. Favier, J. Purseed, and L. Duchemin, *Journal of Fluid Mechanics* **858**, 437–473 (2019).
- [31] L.-A. Couston, E. Hester, B. Favier, J. R. Taylor, P. R. Holland, and A. Jenkins, *Journal of Fluid Mechanics* **911**, A44 (2021).
- [32] E. W. Hester, C. D. McConnochie, C. Cenedese, L.-A. Couston, and G. Vasil, *Phys. Rev. Fluids* **6**, 023802 (2021).
- [33] P. Angot, C.-H. Bruneau, and P. Fabrie, *Numerische Mathematik* **81**, 497 (1999).
- [34] S. Chandrasekhar, *Hydrodynamic and Hydromagnetic Stability* (Dover, 1961).
- [35] P. G. Drazin and W. H. Reid, *Hydrodynamic Stability*, 2nd ed., Cambridge Mathematical Library (Cambridge University Press, 2004).
- [36] D. W. Moore, *Studies in Applied Mathematics* **58**, 119 (1978).
- [37] M. R. Dhanak, *Journal of Fluid Mechanics* **269**, 265–281 (1994).
- [38] S. Grossmann and D. Lohse, *Journal of Fluid Mechanics* **407**, 27–56 (2000).
- [39] X.-L. Qiu and P. Tong, *Phys. Rev. E* **64**, 036304 (2001).
- [40] S. Grossmann and D. Lohse, *Phys. Rev. E* **66**, 016305 (2002).
- [41] T. Moon, D. A. Sutherland, D. Carroll, D. Felikson, L. Kehrl, and F. Straneo, *Nature Geoscience* **11** (2018), 10.1038/s41561-017-0018-z.
- [42] E. G. Josberger and S. Martin, *Journal of Fluid Mechanics* **111**, 439–473 (1981).
- [43] P. Claudin, O. Durán, and B. Andreotti, *Journal of Fluid Mechanics* **832**, R2 (2017).
- [44] M. Bushuk, D. M. Holland, T. P. Stanton, A. Stern, and C. Gray, *Journal of Fluid Mechanics* **873**, 942–976 (2019).